

Tensile properties and strain-hardening behaviour of friction stir welded SiCp/AA2009 composite joints

D.R. Ni^a, D.L. Chen^{b,*}, D. Wang^a, B.L. Xiao^a, Z.Y. Ma^{a,**}

^a Shenyang National Laboratory for Materials Science, Institute of Metal Research, Chinese Academy of Sciences, 72 Wenhua Road, Shenyang 110016, China

^b Department of Mechanical and Industrial Engineering, Ryerson University, 350 Victoria Street, Toronto, Ontario, Canada M5B 2K3

ARTICLE INFO

Article history:

Received 14 February 2014

Received in revised form

10 April 2014

Accepted 16 April 2014

Available online 26 April 2014

Keywords:

Composites

Aluminium alloy

Mechanical properties

Friction stir welding

Joints

Strain hardening

ABSTRACT

3 mm thick rolled 17 vol%SiCp/AA2009 composite sheet in T351 condition (with 15% deformation) was subjected to friction stir welding (FSW). Tensile properties and work hardening behaviour of FSW joints were studied at strain rates from 1×10^{-2} to $1 \times 10^{-5} \text{ s}^{-1}$. The FSW joints tended to fracture in the heat-affected zone, which exhibited the lowest hardness. Joint efficiencies of about 77% were achieved at various strain rates. As the strain rates increased, the yield strength, ultimate tensile strength and elongation decreased slightly, but the effect of strain rate on the elongation became weaker after FSW. The dependence of the strain-hardening exponents on the strain rate was weak in both the base metal (BM) and the FSW joint. Compared to the BM, the FSW joint exhibited higher strain-hardening rates and strain-hardening exponents, as well as a stronger hardening capacity; about three times that of the BM.

© 2014 Elsevier B.V. All rights reserved.

1. Introduction

Due to their superior mechanical and physical properties, metal matrix composites (MMCs) are used in many fields, such as the aerospace and automobile industries [1–3]. Particulate-reinforced aluminium matrix composites (AMCs), especially those reinforced by SiC particles (SiCp), have developed remarkably during the last 30 years due to their excellent properties and relatively low cost. However, the structural application of AMCs involves welding and joining processes and the joining of AMCs by conventional fusion welding techniques is extremely difficult due to the presence of ceramic particles. For fusion welded AMCs, problems such as the presence of porosity, the incomplete mixing of the parent and filler materials and the formation of excess eutectic and deleterious phases could easily occur in the welds [4,5]. Therefore, the development of effective techniques for welding AMCs is required.

Friction stir welding (FSW) is a relatively new solid state joining technique, which was developed by The Welding Institute, UK, in 1991 [6,7]. This technique is termed “green” technology due to its energy efficiency and environmental friendliness. FSW has been successfully used to join aluminium alloys, especially the precipitation-hardened (2xxx, 6xxx, and 7xxx) ones [8–11]. Nowadays, it is also used to weld other alloys with high-melting points and high hardness, such as Cu, Ti

and steel [6]. Additionally, FSW is a promising method for the welding of AMCs, which may avoid the drawbacks of fusion weldings.

Because of the existence of hard and abrasive ceramic particles, it is a great challenge to join AMCs by FSW due to the rapid and severe wear of the normal steel tool [12]. The tool wear could lead to the formation of root flaw defects and deleterious intermetallics which decreased the mechanical properties of the joints [13]. The use of harder tool materials or surface coating in FSW of AMCs could effectively decrease the wear of tool, prolonging the tool life greatly [14,15]. Therefore, increasing attention has been paid to the FSW of AMCs.

FSW has been shown to produce a more homogeneous distribution of the particles, their breakup and bluntness due to severe plastic deformation and material mixing induced by rotating pin. Furthermore, the grain sizes of the matrices were greatly refined due to dynamic recrystallisation. It was reported that AMC joints with good tensile properties could be generated by FSW [16–31], as summarised in Table 1. In some cases, the nugget zone (NZ) of FSW AMC joints even exhibited better tensile strength than the base metal (BM) due to the modified microstructure [21,32–34].

Although several studies on the FSW of AMCs have been reported in the past few years, information on the effect of strain rate on the tensile properties of FSW joints is lacking. Strain-hardening behaviour is one of the important considerations in the evaluation of plastic deformation of materials and it should be evaluated to ensure the integrity and safety of joints and structures. However, studies on the strain-hardening behaviour of FSW joints are limited and focus mainly on magnesium alloys [35–37].

* Corresponding author. Tel.: +1 4169795000x6487; fax: +1 4169795265.

** Corresponding author. Tel./fax: +86 24 83978908.

E-mail addresses: dchen@ryerson.ca (D.L. Chen), zym@imr.ac.cn (Z.Y. Ma).

Table 1
Tensile properties of friction stir welded aluminium matrix composites.

Materials	T, (mm)	D/d (mm)	r/v (rpm/mm min ⁻¹)	Condition	YS (MPa)	UTS (MPa)	El (%)	Eff. (%)	Ref.
10 vol% Al ₂ O ₃ p/AA7005	7.0	18/8	600/300	BM: extruded +T6 joint: FSW	326 263	370 299	4.2 1.2	80	[16]
10 vol% Al ₂ O ₃ p/AA7075	7.0	–	800/56	BM:T6 joint: FSW	290 245	310 260	1.5 0.58	84	[17]
20 vol% Al ₂ O ₃ p/AA6061	7.0	–	800/56	BM: T6 joint: FSW	330 280	379 329	2.1 1.3	87	
20 vol% Al ₂ O ₃ p/AA6061	7.0	20/8	–	BM: extruded +T6 joint: FSW	277 234	355 251	– –	71	[18]
20 vol% Al ₂ O ₃ p/AA6061	7.0	20/8	–	BM: extruded +T6 joint: FSW	340 193	364 262	1.7 2.8	72	[19]
22 vol% Al ₂ O ₃ p/AA6061	4.0	15/4	(630,880)/(115–260)	BM: cast joint: FSW	– –	230 217	– –	94	[20]
15 vol% SiCp/AA2009	8.0	24/8	600/50	BM: extruded Joint: FSW BM: extruded+T4 Joint: FSW+T4	164 236 340 324	305 328 470 445	6.5 2.0 4.0 3.0	100 95	[21][22]
6 vol% B ₄ C/AA6063	4.5	13/4	1500/600	BM: extruded +T5 Joint 1: FSW Joint 2: FSW+aged Joint 3: FSW+T6	241 125 – 184	276 172 223 200	10.1 2.5 0.5 1.1	– 62 81 73	[23]
10.5 vol% B ₄ C/AA6063	4.5	13/4	1500/600	BM: extruded +T5 Joint 1: FSW Joint 2: FSW+aged Joint 3: FSW+T6	253 125 219 136	286 176 238 172	4.2 2.5 1.3 2.4	– 62 84 60	
10 vol% TiB ₂ /Al	6.0	16/5	2000/30	BM: cast joint: FSW	– –	– 223–282	– 3.4–6.7	79–99	[24]
15 vol% Mg ₂ Si/Al	6.0	18/6	1120/125	BM: cast joint: FSW	– –	115 115	– –	100	[25]
3–7 wt% TiCp/AA6061	6.0	–	–	BM: cast Joint: FSW	– –	– –	– –	90–98	[26]
10 wt% ZrB ₂ /AA6061	6.0	18/6	1150/50	BM: cast Joint: FSW	– –	253 240	4.0 1.0	95	[27]
20 wt% AlNp/AA6061	6.0	18/6	1200/55	BM: cast Joint: FSW	– –	241 225	– –	93	[28]
10 vol% SiCp/AA6061	6.0	18/6	1100/45	BM: cast Joint: FSW	200 126	278 206	8.0 6.8	74	[29]
25 vol% SiCp/AA6061	15	20/8	550/75	BM: PM+T6 Joint 1: FSW Joint 2: FSW+T6	657 407 479	742 552 642	5.3 2.6 2.9	– 74.4 86.5	[30]
SiCp/AA2124	–	–	–	BM: hot rolling Joint 1: FSW Joint 2: FSW+T4	– 192 344	– 321 521	– 5.9 7.1	– 100 –	[31]
15 vol% SiCp/AA2009	6.0	20/8	800/100	BM: hot rolling Joint 1: FSW BM+T4	– 192 357	– 321 543	– 5.9 13.1	– 100 –	
17 vol% SiCp/AA2009	3.0	14/5	1000/50	BM: rolled+T351 joint: FSW	508 278	581 443	4.3 4.7	77	Present

T: thickness of plate; D/d: shoulder diameter/Pin diameter; r/v: rotation rate/welding speed; Joint eff.: UTS_{joint}/UTS_{BM}.

In our previous investigation, the microstructure evolution of a FSW SiCp/AA2009-T351 composite sheet was carefully studied [38], and the FSW joint exhibited good fatigue properties [39]. In this work, the tensile properties of the FSW joints were determined at various strain rates with the aim to evaluate the effect of strain rate on the tensile properties and the strain-hardening behaviour of FSW joints.

2. Material and methods

3 mm thick 17 vol% SiCp (average particle size of 7 μm) reinforced AA2009 matrix composite, produced by powder metallurgy technique, was used for FSW. The nominal chemical composition of the AA2009 alloy was 4.26Cu–1.61Mg–0.01Si–0.009Fe (wt%). The hot pressed ingot was extruded and subsequently rolled into a sheet 3 mm thick. The rolled sheet was T351-treated before FSW (solutionised at 502 °C for 1 h, water quenched, cold rolled with 15% deformation and then aged at room temperature for more than one month).

The composite pieces were subjected to FSW perpendicular to the rolling direction at a tool rotational rate of 1000 rpm and a

welding speed of 50 mm min⁻¹. A cermet tool with a concave shoulder 14 mm in diameter and a cylindrical pin 5 mm in diameter and 2.7 mm in length was used, where the pin had a triangular tip without threads.

Following FSW, the welded sheet was maintained at room temperature for one month to age naturally. The specimens for microstructural examination were cross-sectioned perpendicular to the direction of FSW. The microstructures were examined by optical microscopy (OM) without etching and by transmission electron microscopy (TEM, FEI TECNAIG20). Thin foils for TEM were cut from the BM, NZ and heat-affected zone (HAZ).

The hardness profiles were measured along the mid-thickness of the sheet at an interval of 0.5 mm on the cross section of the weld, by using a computerised Buehler hardness tester (Buehler, Lake Bluff, IL) under a load of 1000 g for 15 s. Tensile specimens with a parallel section of 32 × 5.6 × 3 mm³ were machined perpendicular to the direction of FSW. The specimens were electrical discharge machined and ground with SiC papers up to grit #600 to achieve a smooth surface. Tensile tests were conducted at constant strain rates of 1 × 10⁻², 1 × 10⁻³, 1 × 10⁻⁴ and 1 × 10⁻⁵ s⁻¹ at room temperature. At least two specimens were tested at each strain rate. After the tensile tests, the fracture surfaces were

examined using SEM (JEOL JSM-6380LV) coupled with an energy-dispersive X-ray spectroscopy (EDS) system.

3. Results

3.1. Microstructure

A typical cross-sectional view of the FSW SiCp/AA2009 joint is shown in Fig. 1. The joint consisted of four zones: the NZ, the thermomechanically-affected zone (TMAZ), the HAZ and the BM. No defects were observed in the weld. This indicates that a sound joint was achieved. The NZ exhibited a basin shape without onion rings, which are features typically observed in the cross-sections of the NZ in FSW aluminium alloys.

The OM microstructures of the FSW joint are shown in Fig. 2. In the BM, SiCp were homogeneously distributed in the matrix and showed a polygonal morphology (Fig. 2a and c). After FSW, the distribution of SiCp was basically unchanged in the NZ. However, the edges and corners of some SiCp became blunted (Fig. 2b and d).

The TEM microstructures of the BM, NZ and HAZ are shown in Fig. 3. In the BM, a high density of dislocations was observed but no precipitates were detected (Fig. 3a). However, a lower density of dislocations and a few coarse precipitates were seen in the NZ (Fig. 3b). Unlike in the BM and the NZ, few dislocations but many coarse precipitates were observed in the HAZ (Fig. 3c). These



Fig. 1. Cross-sectional view of FSW SiCp/AA2009 joint.

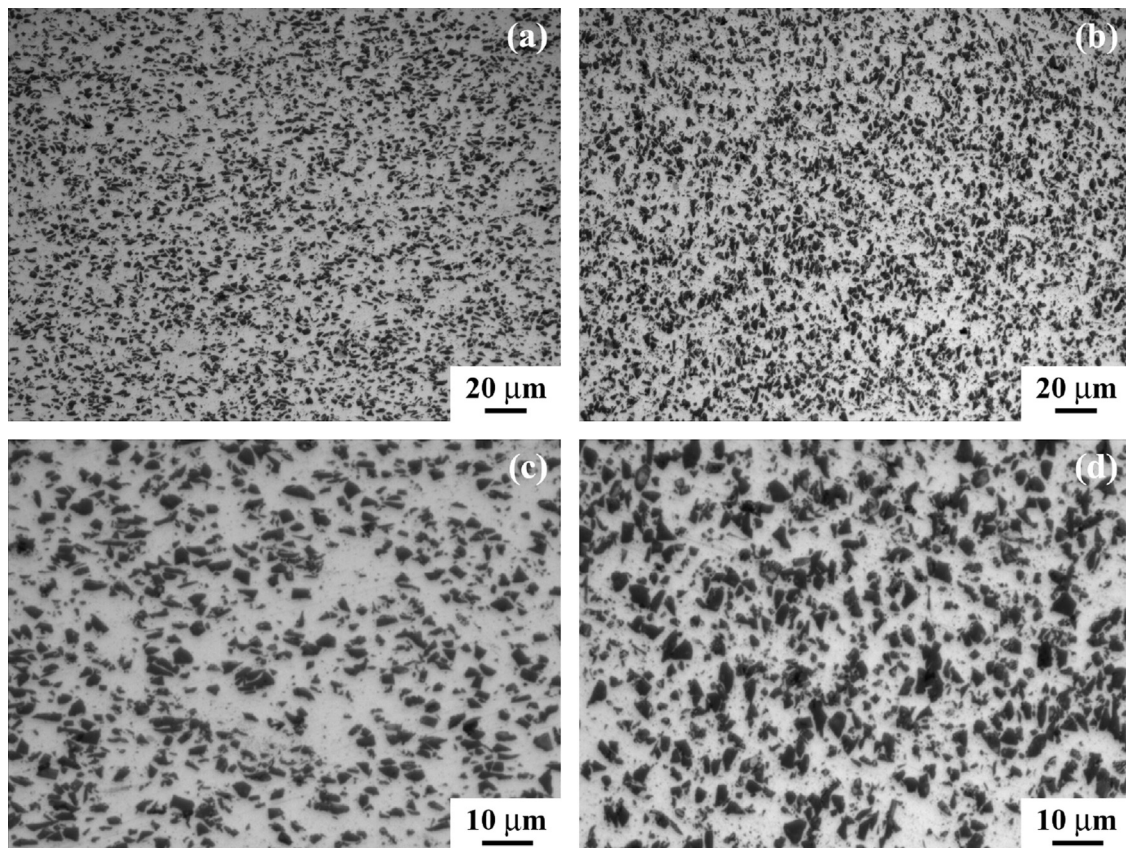


Fig. 2. Optical microstructures of FSW SiCp/AA2009 joint: (a) BM and (b) NZ, showing distribution of SiCp at lower magnification; (c) BM and (d) NZ, showing morphology of SiCp at higher magnification.

precipitates could be divided into two kinds according to their morphologies and sizes: fine needle-shaped precipitates and coarse granular precipitates. According to other studies [21,40,41], the fine needle-shaped precipitates should be S phase (Al_2CuMg), whereas the coarse granular precipitates should be θ (Al_2Cu).

3.2. Microhardness

The hardness profile on the cross section along the mid-thickness of the FSW SiCp/AA2009 composite is shown in Fig. 4. The hardness of the BM and the NZ was about 200 HV and 160 HV, respectively. The lowest hardness, about 130–135 HV, was observed in the HAZ on both the retreating side (RS) and the advancing side (AS); the RS showed a slightly lower hardness than the AS. It has been documented that the hardness profile of FSW heat-treatable aluminium alloys depends greatly on the precipitate distribution [42]. As presented above, a few coarse θ phases were observed in the NZ. Therefore, this region showed a lower hardness than the BM. However, many coarse S and θ phases appeared in the HAZ, resulting in the lowest hardness of the joint.

3.3. Tensile properties

On a macroscopic scale, both the SiCp/AA2009 BM and the FSW joint exhibited limited ductility of 3–5%. For the BM, the fracture surfaces were normal to the tensile stress axis (not shown). In the case of the FSW joint, the fracture of all samples occurred in the HAZ with most of the failures being located on the RS (Fig. 5). Fig. 6 shows typical true stress versus true strain curves of the BM and the FSW joints tested at various strain rates. Compared with the BM, the FSW joint showed apparently lower yield strength

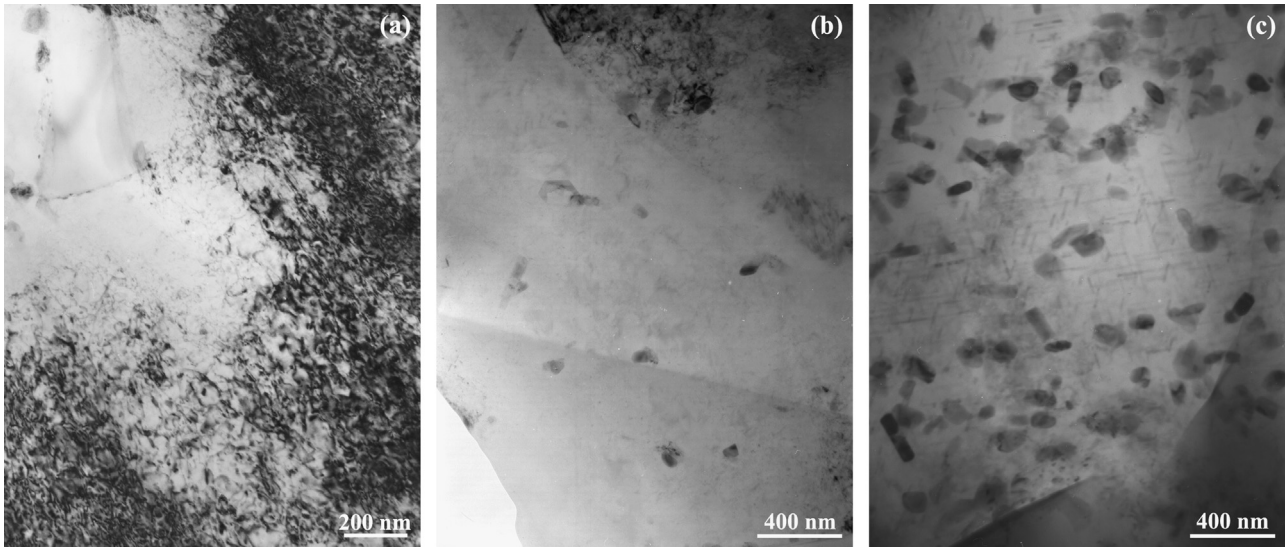


Fig. 3. TEM microstructures of FSW SiCp/AA2009 joint: (a) BM, (b) NZ, and (c) HAZ.

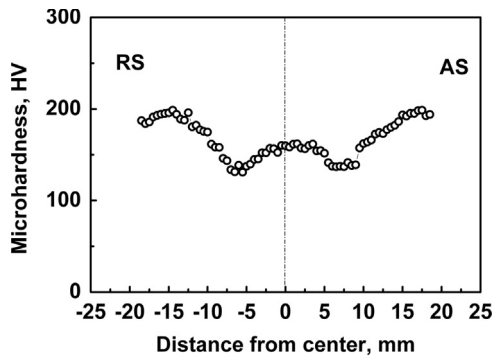


Fig. 4. Typical microhardness profile of FSW SiCp/AA2009 joint.

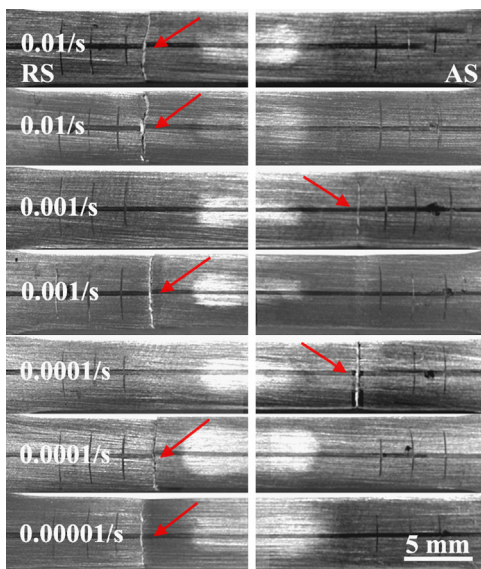


Fig. 5. Optical micrographs showing the upper surface of FSW SiCp/AA2009 joints tested at various strain rates, arrows showing failure locations.

(YS) and ultimate tensile strength (UTS) but better ductility. Fig. 7 shows that for both the BM and the FSW joint, while the UTS slightly decreased as the strain rate increased, the YS appeared to be independent of the strain rate and the effect of strain rate on

the ductility became weaker after FSW. An average joint efficiency of about 77% was obtained at the various strain rates.

3.4. Fractograph

Fig. 8 shows typical fractographs of the BM tested at strain rates of $1 \times 10^{-2} \text{ s}^{-1}$ and $1 \times 10^{-5} \text{ s}^{-1}$. The overall view shows that the fracture surfaces were rough and wavelike and the initiation of cracks was located at the sample surfaces (Fig. 8a and d). At a higher magnification, the initiation zone was characterised by pits and fractured SiCp (Fig. 8b and e), showing a typical fracture surface of the AMCs. Large and shallow Al dimples together with some microcracks were observed on the fracture surfaces and some cracked SiCp were observed at the bottom of the dimples (Fig. 8c and f). Generally, little difference was observed in the features of the fracture surfaces between the two strain rates.

Fig. 9 shows typical fractographs of the FSW SiCp/AA2009 joint tested at strain rates of $1 \times 10^{-2} \text{ s}^{-1}$ and $1 \times 10^{-5} \text{ s}^{-1}$. The FSW joint showed quite different fracture surfaces compared with those of the BM, shown in Fig. 8. These fracture surfaces were smoother without evident initiations (Fig. 9a and d). At a higher magnification, many fine Al dimples and broken SiCp were observed and the fracture surface exhibited morphology typical of ductile fracture (Fig. 9b and e). Furthermore, the dimples were smaller but their quantity was greater compared with those of the BM. Pull-out marks of SiCp were also observed but fewer cracks were visible (Fig. 9c and f). The effect of strain rate on the fracture characteristics of the FSW joint was also weak and the fracture surfaces showed similar morphologies at both low and high strain rates.

4. Discussion

4.1. Microstructure

It seemed that the distribution of SiCp was not visibly improved and this could be ascribed to the fact that the SiCp have already been homogeneously distributed in the BM (Fig. 2). Due to the intense deformation and mixing during FSW, some large SiCp in the NZ were broken; meanwhile, the rotating pin also knocked off the corners and sharp edges from the large SiCp and thus, blunted the sharp SiCp (Fig. 2). It was reported that the dynamically

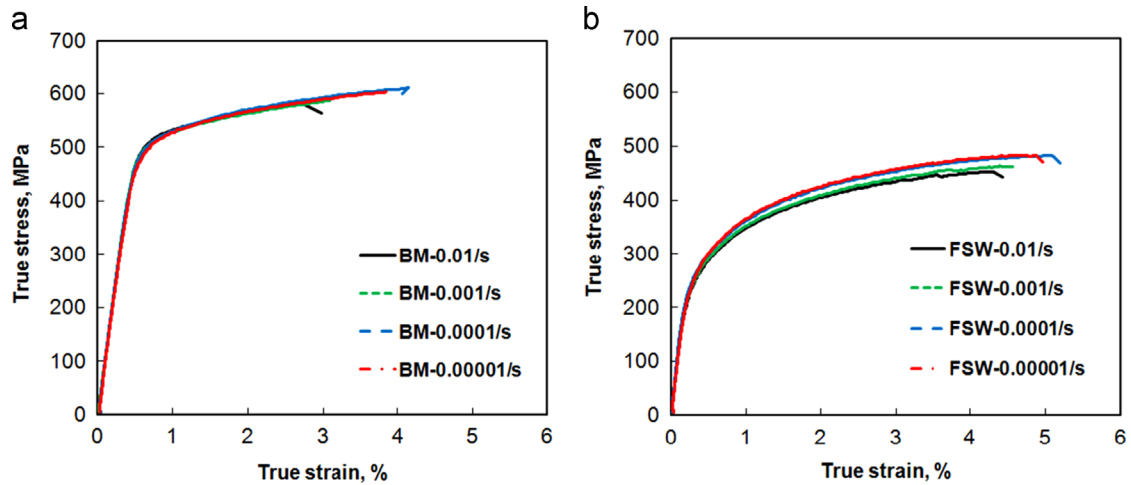


Fig. 6. Typical true stress–true strain curves of SiCp/AA2009 BM and FSW joints at various strain rates.

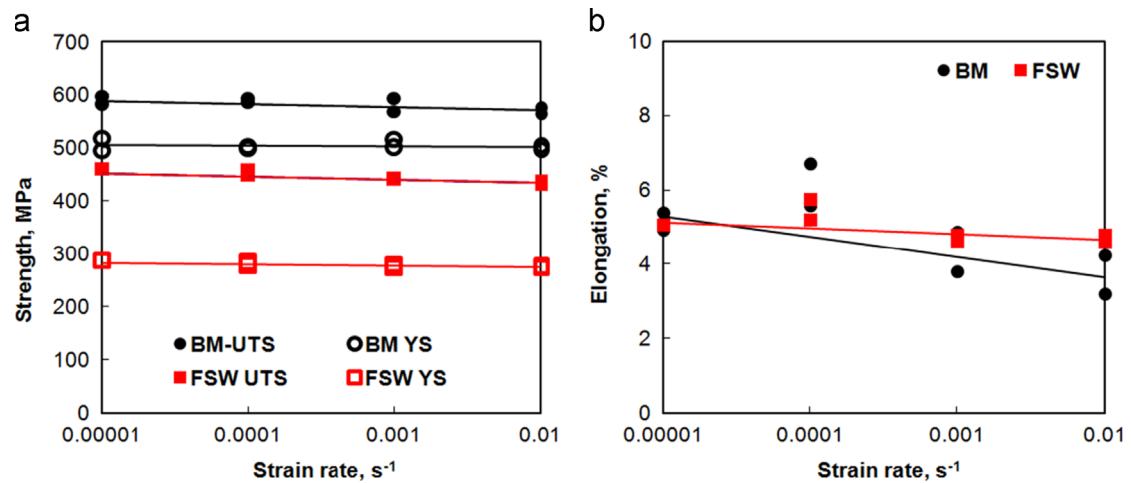


Fig. 7. Effect of strain rate on (a) strength and (b) ductility of SiCp/AA2009 BM and FSW joints.

recrystallised Al grains nucleated on the surface of fractured SiCp during FSW, and these clean interfaces were beneficial to the load transfer between SiCp and Al matrix [43].

The fabrication and microstructure of SiCp/Al–Cu–Mg composites were reported in detail in previous references [44–47]. The precipitation sequences of the Al–Cu–Mg alloys are extremely complex and can be divided into two kinds depending on the Cu/Mg ratio [42,48,49]. For the naturally aged (T4) Al–Cu–Mg alloys, the dominant strengthening phases are GPB zones, which are considered to be a short-range ordering of Cu and Mg solute atoms and have cylindrical shapes with sizes of about several nanometres and are difficult to detect even by TEM [47]. Meanwhile, it is well established that the S phase (Al_2CuMg) and θ phase (Al_2Cu) are two types of stable precipitates in the over-aged Al–Cu–Mg alloys. The TEM results showed no visible precipitates in the BM but a few coarse θ existed in the NZ and many coarse needle-shaped S and coarse granular θ existed in the HAZ (Fig. 3).

FSW can be considered a complicated hot-working process [21]. This process initially dissolves the precipitates into the Al matrix in the NZ. During the cooling from the FSW temperature, part of the dissolved precipitates re-precipitate out in the NZ to form the θ phase, due to the slow cooling rate. Many S and θ phases were observed in the HAZ and this was due to the coarsening of the precipitates during the FSW thermal cycle.

Due to the large coefficient of thermal expansion (CTE) mismatch strain between the Al matrix and SiCp [50], the water

quenching process induces a high dislocation density in the BM (Fig. 3a). The lower dislocation density in the NZ results from the dynamic recrystallisation process and the slow cooling rate in the air. The dislocations are greatly reduced in the HAZ and this is attributed to the dislocation release resulting from the FSW thermal cycle.

4.2. Tensile properties

For the FSW joint, fracture occurred in the HAZ with most of the failure locations on the RS (Fig. 5). This is in agreement with the hardness profiles of the joint (Fig. 4). The fracture surfaces of the BM showed little difference at various strain rates, as did the FSW joint and this may be attributed to their low ductility.

The tensile testing results showed the FSW joint exhibited apparently lower YS and UTS than the BM but it showed better ductility. Table 1 shows that the joint efficiency of FSW AMC joints was greatly influenced by the initial condition of the BM and the final condition of the FSW joints. Furthermore, a proper heat-treatment process may greatly improve the strength of the FSW joints. For the relatively soft composites in the as-cast state, the FSW joint efficiency could reach nearly 100% [24–26]. However, for the heat-treated extruded composites, which exhibit relatively higher strength, the strength of FSW joints is apparently lower than that of the BM.

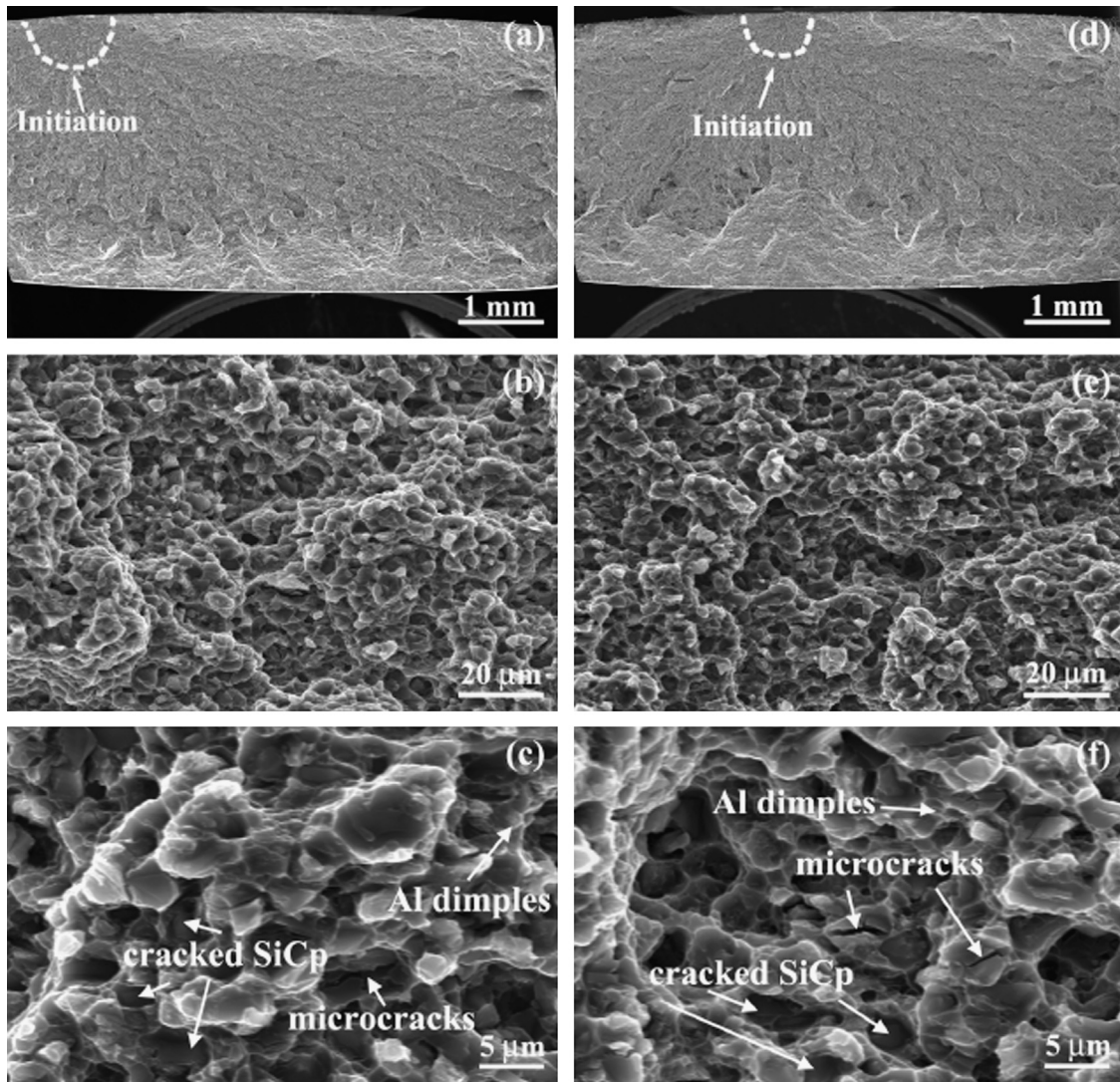


Fig. 8. SEM fractographs of BM at strain rates of (a–c) $1 \times 10^{-2} \text{ s}^{-1}$ and (d–f) $1 \times 10^{-5} \text{ s}^{-1}$: (a) and (d) overall view at lower magnification; (b) and (e) initiation site at higher magnification; (c) and (f) details of initiation site.

Ceschini et al. [16,19] reported that the efficiency of the FSW joints was about 80% and 72% for the extruded 10 vol% $\text{Al}_2\text{O}_3\text{p}/\text{AA7005-T6}$ and 20 vol% $\text{Al}_2\text{O}_3\text{p}/\text{AA6061-T6}$ composites, with the UTS decreased from 370 to 299 MPa and from 364 to 262 MPa, respectively. The result of the latter material was similar to that reported by Marzoli et al. [18]. Cavaliere et al. [17] reported that the efficiency of the FSW joints was about 84% and 87% for the extruded 10 vol% $\text{Al}_2\text{O}_3\text{p}/\text{AA7075-T6}$ and 20 vol% $\text{Al}_2\text{O}_3\text{p}/\text{AA6061-T6}$ composites, with the UTS decreased from 310 to 260 MPa and from 379 to 329 MPa, respectively. Chen et al. [23] reported that the efficiency of the FSW joints was about 62% for the extruded 6 vol% and 10.5 vol% $\text{B}_4\text{C}/\text{AA6063-T5}$ composites, with the UTS decreased from 276 to 172 MPa and from 286 to 176 MPa, respectively, but the joint efficiency could increase to over 80% after an artificial aging process. Table 1 also shows that the FSW joints of the heat-treated extruded composites generally exhibited low ductility with most of the elongations below 2.8%.

In the present study, the FSW joint of the as-rolled $\text{SiCp}/\text{AA2009}$ showed superior strength and ductility compared with previous results. The lower strength of the FSW joint than that of the BM is attributed to the softening of the HAZ. Both the BM and the FSW joint showed decreased strength and ductility with

increasing strain rate. However, the effect of strain rate on the ductility became smaller after FSW.

4.3. Strain-hardening behaviour

The hardening capacity (Hc) of a material may be considered as a ratio of the ultimate tensile strength (σ_{UTS}) to the yield strength (σ_y) [51]. Afrin et al. [35] re-defined a normalised parameter of hardening capacity as

$$Hc = (\sigma_{\text{UTS}} - \sigma_y) / \sigma_y = \sigma_{\text{UTS}} / \sigma_y - 1 \quad (1)$$

The hardening capacity of the BM and the FSW joint at various strain rates is shown in Table 2. Two important findings can be observed from Table 2. First, the hardening capacity of both the BM and the FSW joint varied slightly with increasing strain rate. Second, the FSW joint showed an obviously higher hardening capacity of about three times that of the BM.

Several equations have been proposed to evaluate the strain-hardening exponent of a material [35,36,52,53], as follows:

$$\sigma = K\epsilon^n \quad (2)$$

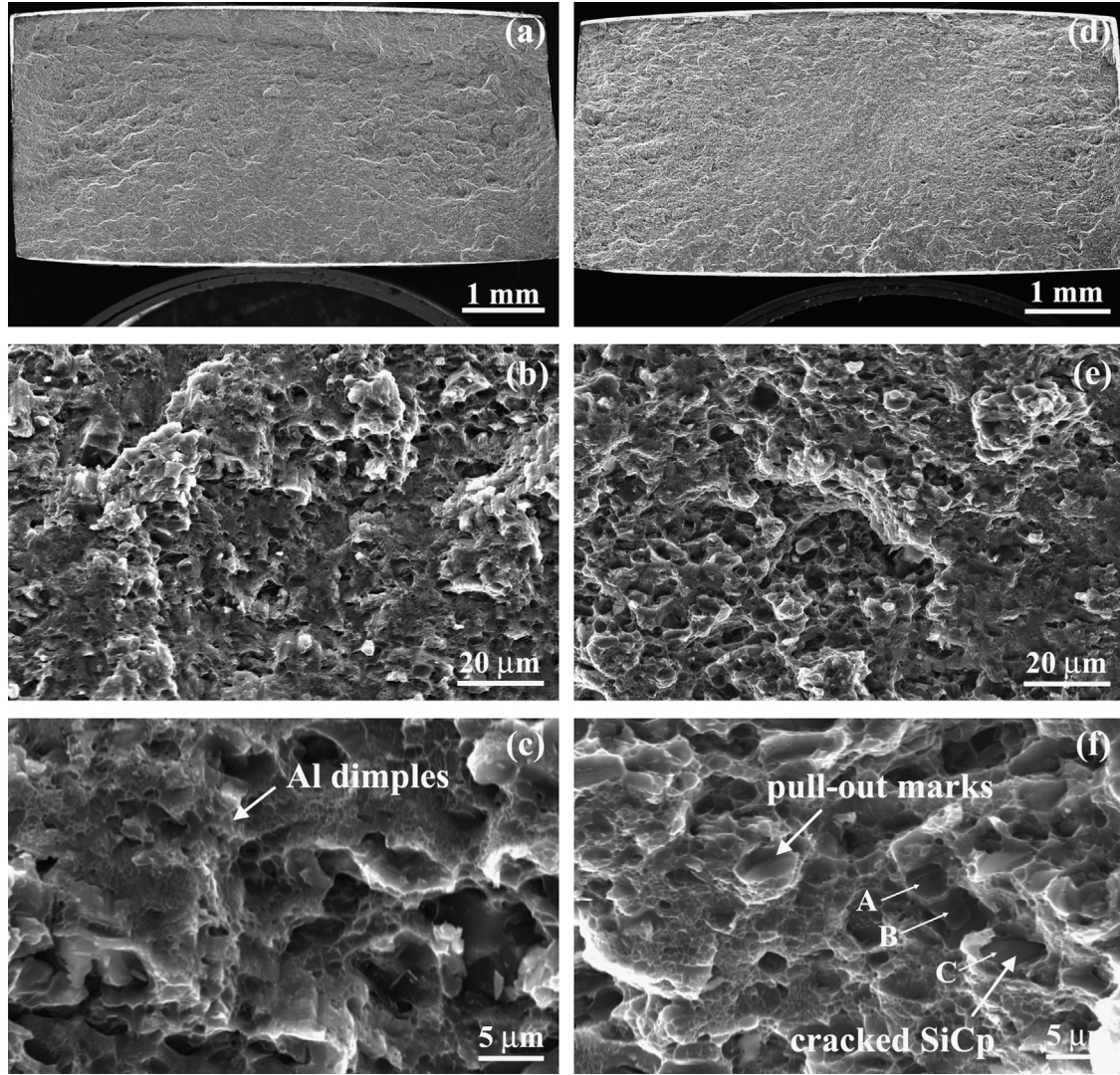


Fig. 9. SEM fractographs of FSW SiCp/AA2009 joints at strain rates of (a–c) $1 \times 10^{-2} \text{ s}^{-1}$ and (d–f) $1 \times 10^{-5} \text{ s}^{-1}$: (a) and (d) overall view at lower magnification; (b) and (e) initiation site at higher magnification; (c) and (f) details of initiation site.

Table 2
Hardening capacity of BM and FSW joint tested at various strain rates.

Sample	Strain rate (s^{-1})	Hardening capacity
BM	1×10^{-2}	0.14
	1×10^{-3}	0.14
	1×10^{-4}	0.18
	1×10^{-5}	0.16
FSW joint	1×10^{-2}	0.58
	1×10^{-3}	0.60
	1×10^{-4}	0.62
	1×10^{-5}	0.61

$$\sigma = \sigma_y + K_1 \epsilon^{n_1} \quad (3)$$

$$\sigma = \sigma_y + K^* (\epsilon - \epsilon_y)^{n^*} \quad (4)$$

In Eq. (2) [52], σ , ϵ , K and n are the true stress, true strain, strength coefficient and strain- (or work-) hardening exponent, respectively. In Eq. (3) [53], n_1 is the strain-hardening exponent and σ_y is the yield strength; K_1 is the strength coefficient which represents the increment in strength due to the strain hardening at $\epsilon=1$. In Eq. (4) [35], n^* , σ , ϵ and ϵ_y are the strain-hardening exponent, true

stress, true strain and yield strain of a material, respectively; K^* is the strength coefficient which reflects the increment in strength due to strain hardening corresponding to $(\epsilon - \epsilon_y) = 1$.

Fig. 10 shows the evaluated strain-hardening exponents (n , n_1 , n^*) as a function of strain rate for the BM and the FSW joint. The effect of strain rate on the strain-hardening exponents is weak in both the BM and the FSW joint. The n -value is about 0.09 and 0.21 for the BM and the FSW joint, respectively, and the FSW joint exhibits a much higher n -value than the BM (Fig. 10a). The n_1 -value is about 1.0 for both the BM and the FSW joint and it increases slightly with increasing strain rates (Fig. 10b). The n^* -value is about 0.54 and 0.63 for the BM and the FSW joint, respectively, and the FSW joint exhibits a slight higher n^* -value than the BM (Fig. 10c). This is related to the greatly lower YS of the FSW joint. It is also seen that the n values are the smallest and n_1 values are the highest with n^* lying in between the two. Similar results were also reported in magnesium alloys [35,36].

Fig. 11 shows a typical Kocks–Mecking plot of strain-hardening rate ($\theta = d\sigma/d\epsilon$) versus net flow stress ($\sigma - \sigma_y$) at the various strain rates for the BM and the FSW joint. No stage I hardening (depending on the crystal orientation) or stage II hardening (strain-hardening rate being constant) are observed in either the BM or the FSW joint and stage III hardening (strain-hardening rate decreasing linearly with increasing net flow stress) appears

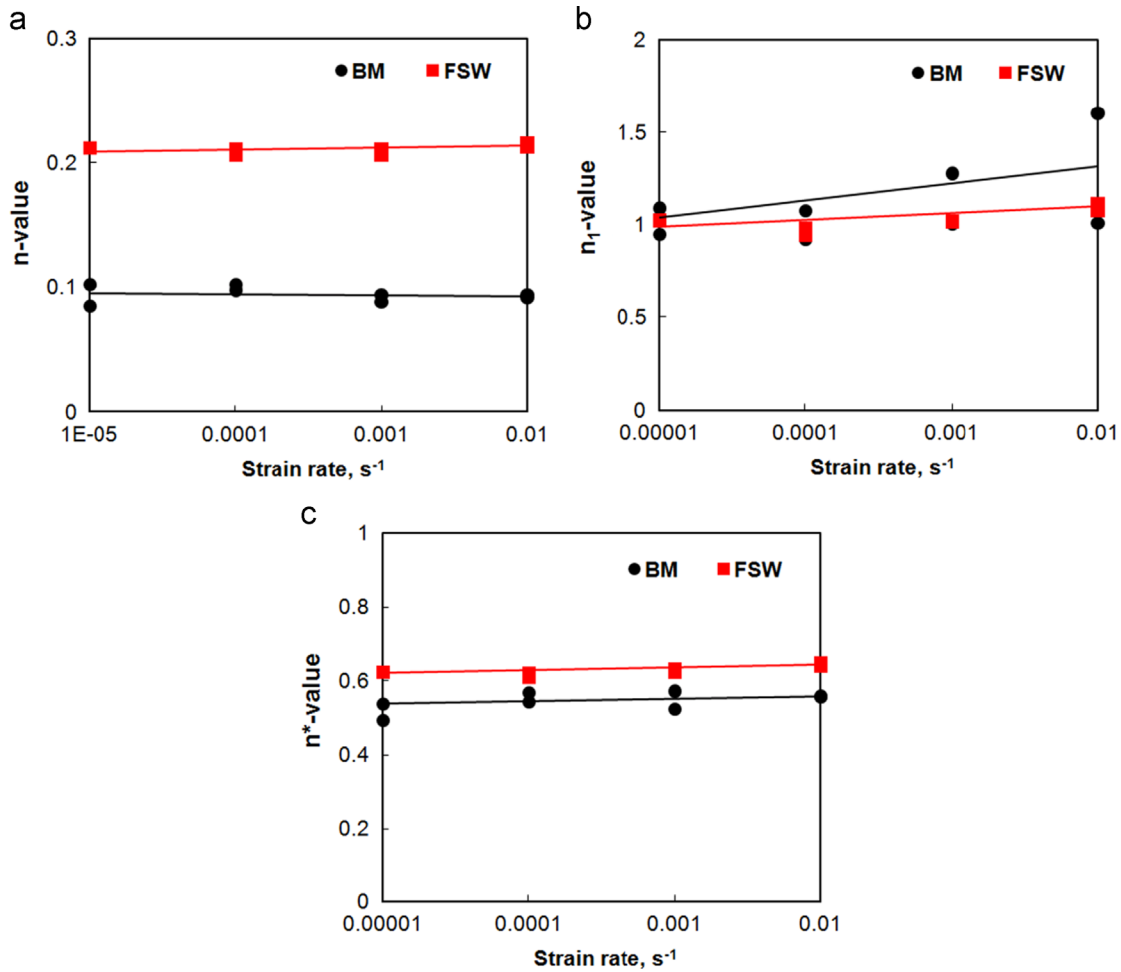


Fig. 10. Effect of strain rate on strain-hardening exponent of SiCp/AA2009 BM and FSW joints: (a) n -value, (b) n_1 -value, and (c) n^* -value.

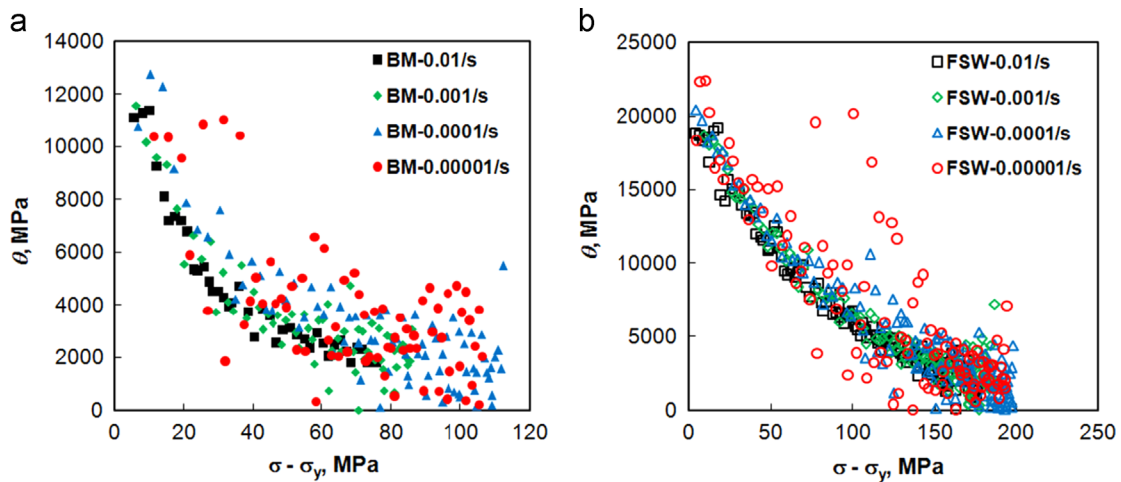


Fig. 11. Strain-hardening rate (θ) versus net flow stress ($\sigma - \sigma_y$) of SiCp/AA2009 BM and FSW joints at various strain rates.

immediately after yielding. As can be seen, stage III is weakly strain-rate sensitive in both the BM and the FSW joint. However, the FSW joint shows a much higher strain-hardening rate and a higher hardening capacity than the BM. When the true stress exceeds a certain value, stage IV occurs. It is seen that stage IV in the FSW joint both appears and ends later compared with that in the BM. This is different from that of FSW Mg alloys, in which stage IV appeared to be similar in both BM and FSW joints [36,37].

The strain-hardening behaviour of metals is affected mainly by grain size and dislocation density [36,37]. For FSW joints, the grain refinement in the NZ is beneficial to the strain hardening. Meanwhile, as discussed above, the NZ shows a lower dislocation density than the BM due to the dynamic recrystallisation and the slow cooling rate. Therefore, this kind of microstructure would store more new dislocations that were generated during plastic deformation. Moreover, during the tension, most of the deformations happened in the HAZ,

Table 3
Results of EDS analysis in Fig. 9f (wt%).

Location	Al	Si	Cu	Mg	C	O
Point A	77.9	3.9	2.6	0.9	11.2	3.5
Point B	65.4	11.6	2.9	1.4	15.7	3.0
Point C	40.5	29.7	1.3	0.7	27.8	–

which showed the lowest dislocation density and this could be particularly responsible for the better strain-hardening behaviour of the FSW joint.

Afrin et al. [35] reported that the strain-hardening exponent of an FSW AZ31B alloy was nearly three times higher than that of the BM and the hardening capacity was about twice that of the BM. Chowdhury et al. [36,37] studied the strain-hardening behaviour of a double-sided arc welded and FSW AZ31B alloy. They reported that the strain-hardening exponents were nearly twice that of the BM and the double-sided arc welded samples exhibited stronger strain-hardening capacity than the FSW samples and the BM. As discussed above, the FSW increased the strain-hardening exponent and strain-hardening capacity of the AMC and this result is similar to that of FSW magnesium alloys [35–37].

4.4. Fractograph

For the BM, the initiation of cracks was located at the sample surfaces (Fig. 8a and d). The fractured SiCp indicated the excellent interfacial bonding between SiCp and matrix (Fig. 8b and e). The Al dimples, microcracks and cracked SiCp indicated that the BM failed mainly in the form of both ductile failure of the matrix and fracture of SiCp (Fig. 8c and f). This is why the present 17 vol% SiCp/AA2009 composite exhibited a YS as high as 500 MPa and a UTS reaching 580 MPa (Table 1). The FSW joint showed quite different fracture surfaces compared with the BM. The features of the fracture surface suggest that the fracture process of the FSW joint was controlled not only by the ductile failure of the matrix in conjunction with the fracture of SiCp but also by the SiCp pull-out, where the HAZ exhibited better ductility than the BM (Fig. 9b and e). The pull-out of SiCp revealed the occurrence of particle-matrix debonding (Fig. 9c and f). The results of EDS analysis (Table 3) show that points A and B in Fig. 9f contained more Al and less Si, so that they should be the pulled-out SiCp. Point C contained more Si and C and it should be a broken SiC particle. The SiCp pull-out was due to the softening of the HAZ where the Al matrix had less constraint to the SiCp.

Srivatsan et al. [50] studied the fracture behaviour of a SiCp/AA2009 composite. They reported that the fracture surface was characterised by cracking of individual and clustered SiCp and considered that the fracture of the Al matrix between the clusters of SiCp, coupled with SiCp failure by cracking and decohesion at the Al–SiCp interfaces, resulted in the low tensile ductility and the failure of the composite. Basically, the fracture surfaces of the BM in the present study (Fig. 8) showed similar features to those reported by Srivatsan et al. [50].

5. Conclusions

In summary, the following conclusions are reached:

1. A sound FSW weld of SiCp/AA2009-T351 (with 15% deformation) was achieved. The HAZ was characterised by a great number of coarsened precipitates and greatly decreased dislocation density, showing the lowest hardness.

2. At various strain rates, the tensile fracture of the FSW joints occurred in the HAZ with most of them on the RS. The FSW joint showed lower YS and UTS but higher ductility than the BM, with a joint efficiency of ~77%. The YS, UTS and elongation decreased slightly as the strain rate increased but the effect of strain rate on the elongation became weaker after FSW.
3. The effect of strain rate on the strain-hardening exponent was weak in both the BM and FSW joint. The three kinds of strain-hardening exponents n -value, n_1 -value and n^* -value were about 0.09, 1.0 and 0.54 for the BM, respectively and 0.21, 1.0, and 0.63 for the FSW joint, respectively. Compared with the BM, the FSW joint showed much higher strain-hardening rate and three times the hardening capacity due to the higher dislocation storage capacity.
4. The fracture surfaces showed similar morphologies at both low and high strain rates for the BM, as did the FSW joint. The fracture of the FSW joint was governed not only by the ductile failure of the matrix, together with SiCp fracture but also by SiCp pull-out.

Acknowledgements

The authors gratefully acknowledge the support of the National Natural Science Foundation of China under Grant no. 51331008, the National Basic Research Program of China under Grant no. 2012CB619600 and the Natural Sciences and Engineering Research Council of Canada (NSERC) in the form of international research collaboration. D.L. Chen is also grateful for the financial support by the Premier's Research Excellence Award (PREA), NSERC-Discovery Accelerator Supplement (DAS) Award, Automotive Partnership Canada (APC), Canada Foundation for Innovation (CFI), and Ryerson Research Chair (RRC) Program. The authors also thank Mr. Q. Li, A. Machin, J. Amankrah, and R. Churaman (Ryerson University, Toronto, ON, Canada) for their assistance in the experiments.

References

- [1] I.A. Ibrahim, F.A. Mohamed, E.J. Lavernia, J. Mater. Sci. 26 (1991) 1137–1156.
- [2] S.J. Xu, B.L. Xiao, Z.Y. Liu, W.G. Wang, Z.Y. Ma, Acta Metall. Sin. 48 (2012) 882–888.
- [3] S.C. Tjong, Z.Y. Ma, Mater. Sci. Eng. R 29 (2000) 49–113.
- [4] D. Storjohann, O.M. Barabash, S.S. Babu, S.A. David, P.S. Sklad, E.E. Bloom, Metall. Mater. Trans. A 36 (2005) 3237–3247.
- [5] X.H. Wang, J.T. Niu, S.K. Guan, L.J. Wang, D.F. Cheng, Mater. Sci. Eng. A 499 (2009) 106–110.
- [6] R.S. Mishra, Z.Y. Ma, Mater. Sci. Eng. R 50 (2005) 1–78.
- [7] R. Nandan, T. DebRoy, H.K.D.H. Bhadeshia, Prog. Mater. Sci. 53 (2008) 980–1023.
- [8] H.L. Hao, D.R. Ni, H. Huang, D. Wang, B.L. Xiao, Z.R. Nie, Z.Y. Ma, Mater. Sci. Eng. A 559 (2013) 889–896.
- [9] Z. Zhang, B.L. Xiao, Z.Y. Ma, J. Mater. Sci. 47 (2012) 4075–4086.
- [10] D. Wang, C.L. Dong, B.L. Xiao, C. Gao, M. He, G.H. Luan, Z.Y. Ma, Acta Metall. Sin. 48 (2012) 1109–1115.
- [11] Z. Zhang, B.L. Xiao, D. Wang, Z.Y. Ma, Metall. Mater. Trans. A 42 (2011) 1717–1726.
- [12] T. Prater, A. Strauss, G. Cook, B. Gibson, C. Cox, Metall. Mater. Trans. A 44 (2013) 3757–3764.
- [13] A.H. Feng, Z.Y. Ma, Scr. Mater. 57 (2007) 1113–1116.
- [14] T. Prater, A. Strauss, G. Cook, B. Gibson, C. Cox, J. Mater. Eng. Perform. 22 (2013) 1807–1813.
- [15] T. Prater, Acta Astronaut. 93 (2014) 366–373.
- [16] L. Ceschini, I. Boromei, G. Minak, A. Morri, F. Tarterini, Compos. Sci. Technol. 67 (2007) 605–615.
- [17] P. Cavaliere, E. Cerri, L. Marzoli, J. Dos Santos, Appl. Compos. Mater. 11 (2004) 247–258.
- [18] L.M. Marzoli, A.V. Strombeck, J.F. Dos Santos, C. Gambaro, L.M. Volpone, Compos. Sci. Technol. 66 (2006) 363–371.
- [19] L. Ceschini, I. Boromei, G. Minak, A. Morri, F. Tarterini, Compos. Part A 38 (2007) 1200–1210.
- [20] G. Minak, L. Ceschini, I. Boromei, M. Ponte, Int. J. Fatigue 32 (2010) 218–226.
- [21] A.H. Feng, B.L. Xiao, Z.Y. Ma, Compos. Sci. Technol. 68 (2008) 2141–2148.

- [22] Z.Y. Ma, A.H. Feng, B.L. Xiao, J.Z. Fan, L.K. Shi, *Mater. Sci. Forum* 539–543 (2007) 3814–3819.
- [23] X.G. Chen, M. da Silva, P. Gougeon, L. St-Georges, *Mater. Sci. Eng. A* 518 (2009) 174–184.
- [24] S.J. Vijay, N. Murugan, *Mater. Des.* 31 (2010) 3585–3589.
- [25] H. Nami, H. Adgi, M. Sharifitabar, H. Shamabadi, *Mater. Des.* 32 (2011) 976–983.
- [26] S. Gopalakrishnan, N. Murugan, *Mater. Des.* 32 (2011) 462–467.
- [27] I. Dinaharan, N. Murugan, *Mater. Sci. Eng. A* 543 (2012) 257–266.
- [28] N. Murugan, B. Ashok Kumar, *Mater. Des.* 51 (2013) 998–1007.
- [29] P. Periyasamy, B. Mohan, V. Balasubramanian, *J. Mater. Eng. Perform.* 21 (2012) 2417–2428.
- [30] F. Cioffi, R. Fernández, D. Gesto, P. Rey, D. Verdera, G. González-Doncel, *Compos. Part A* 54 (2013) 117–123.
- [31] D. Wang, B.L. Xiao, Q.Z. Wang, Z.Y. Ma, *Mater. Des.* 47 (2013) 243–247.
- [32] M. Amirizad, A.H. Kokabi, M. Abbasi Gharacheh, R. Sarrafi, B. Shalchi, M. Azizieh, *Mater. Lett.* 60 (2006) 565–568.
- [33] F. Khodabakhshi, H. Ghasemi Yazdabadi, A.H. Kokabi, A. Simchi, *Mater. Sci. Eng. A* 585 (2013) 222–232.
- [34] A.M. Hassan, T. Qasim, A. Ghaithan, *Mater. Manuf. Process.* 27 (2012) 1397–1401.
- [35] N. Afrin, D.L. Chen, X. Cao, M. Jahazi, *Scr. Mater.* 57 (2007) 1004–1007.
- [36] S.M. Chowdhury, D.L. Chen, S.D. Bhole, X. Cao, E. Powidajko, D.C. Weckman, Y. Zhou, *Mater. Sci. Eng. A* 527 (2010) 2951–2961.
- [37] S.M. Chowdhury, D.L. Chen, S.D. Bhole, X. Cao, *Mater. Sci. Eng. A* 527 (2010) 6064–6075.
- [38] D.R. Ni, D.L. Chen, D. Wang, B.L. Xiao, Z.Y. Ma, *Mater. Des.* 51 (2013) 199–205.
- [39] D.R. Ni, D.L. Chen, B.L. Xiao, D. Wang, Z.Y. Ma, *Int. J. Fatigue* 55 (2013) 64–73.
- [40] P. Rodrigo, P. Poza, M.V. Utrilla, A. Ureña, *J. Alloys Compd.* 482 (2009) 187–195.
- [41] P.I. Gouma, D.J. Lloyd, M.J. Mills, *Mater. Sci. Eng. A* 319–321 (2001) 439–442.
- [42] C. Genevois, A. Deschamps, A. Denquin, B.D. Cottignies, *Acta Mater.* 53 (2005) 2447–2458.
- [43] D. Wang, B.L. Xiao, Q.Z. Wang, Z.Y. Ma, *J. Mater. Sci. Technol.* 30 (2014) 54–60.
- [44] P. Jin, B.L. Xiao, Q.Z. Wang, Z.Y. Ma, Y. Liu, S. Li, *J. Mater. Sci. Technol.* 27 (2011) 518–524.
- [45] P. Jin, B.L. Xiao, Q.Z. Wang, Z.Y. Ma, Y. Liu, S. Li, *Mater. Sci. Eng. A* 528 (2011) 1504–1511.
- [46] Q. Zhang, B.L. Xiao, Z.Y. Liu, Z.Y. Ma, *J. Mater. Sci.* 46 (2011) 6783–6793.
- [47] Q. Zhang, Q.Z. Wang, B.L. Xiao, Z.Y. Ma, *Acta Metall. Sin.* 48 (2012) 135–141.
- [48] P. Ratchev, B. Verlinden, P. De Smet, P. Van Houtte, *Acta Mater.* 46 (1998) 3523–3533.
- [49] S.C. Wang, M.J. Starink, *Int. Mater. Rev.* 50 (2005) 193–215.
- [50] T.S. Srivatsan, M. Al-Hajri, C. Smith, M. Petraroli, *Mater. Sci. Eng. A* 346 (2003) 91–100.
- [51] J. Luo, Z. Mei, W. Tian, Z. Wang, *Mater. Sci. Eng. A* 441 (2006) 282–290.
- [52] J.H. Hollomon, *Trans. AIME* 162 (1945) 268–290.
- [53] X.H. Chen, L. Lu, *Scr. Mater.* 57 (2007) 133–136.